Available online at www.sciencedirect.com
ScienceDirect
Journal of Environmental Sciences 2012, 24(3) 449–457
JOURNAL OF ENVIRONMENTAL SCIENCES
ISSN 1001-0742
CN 11-2629/X
www.jesc.ac.cn

Hydrothermal fabrication and visible-light-driven photocatalytic properties of bismuth vanadate with multiple morphologies and/or porous structures for Methyl Orange degradation

Haiyan Jiang[1], Hongxing Dai[1,*], Xue Meng[1], Lei Zhang[1], Jiguang Deng[1], Yuxi Liu[1], Chak Tong Au[2]

1. Laboratory of Catalysis Chemistry and Nanoscience, Department of Chemistry and Chemical Engineering, College of Environmental and Energy Engineering, Beijing University of Technology, Beijing 100124, China. E-mail: hxdai@bjut.edu.cn
2. Department of Chemistry, Centre for Surface Analysis and Research, Hong Kong Baptist University, Kowloon Tong, Hong Kong, China

Received 10 April 2011; revised 11 June 2011; accepted 21 June 2011

Abstract

Monoclinic $BiVO_4$ with multiple morphologies and/or porous structures were fabricated using the hydrothermal strategy. The materials were characterized by means of the XRD, Raman, TGA/DSC, SEM, XPS, and UV-Vis techniques. The photocatalytic activities of the $BiVO_4$ materials were evaluated for the degradation of Methyl Orange under visible-light irradiation. It is observed that pH value and surfactant exerted a great effect on the morphology and pore structure of the $BiVO_4$ product. Spherical $BiVO_4$ with porous structures, flower-cluster-like $BiVO_4$, and flower-bundle-like $BiVO_4$ were generated hydrothermally at 100°C with poly(vinyl pyrrolidone) (PVP) and urea (pH = 2) and at 160°C with $NaHCO_3$ (pH = 7 and 8), respectively. The PVP-derived $BiVO_4$ showed much higher surface areas (5.0–8.4 m^2/g) and narrower bandgap energies (2.45–2.49 eV). The best photocatalytic performance of the spherical $BiVO_4$ material with a surface area of 8.4 m^2/g was associated with its higher surface area, narrower bandgap energy, higher surface oxygen vacancy density, and unique porous architecture.

Key words: visible-light-driven catalyst; porous bismuth vanadate; hydrothermal fabrication; Methyl Orange degradation; photocatalysis

DOI: 10.1016/S1001-0742(11)60793-6

Introduction

Semiconductor photocatalysis is one of the most promising technologies for solar energy utilization and environmental remediation (Ai et al., 2009). TiO_2 has been proven to be photocatalytically active for the degradation of organic pollutants (Hoffmann et al., 1995; Chen and Dionysiou, 2006). However, TiO_2 responds only to ultraviolet light, which represents a small fraction (ca. 4%) of the sunlight energy. Therefore, it is highly required to develop visible-light-driven photocatalytic materials.

As one of the Ti-free semiconductor photocatalysts, bismuth vanadate has recently attracted much attention due to its photocatalytic activity (Xu et al., 2008). For example, $BiVO_4$ with different particle sizes and morphologies showed good photocatalytic performance for the degradation of Methyl Orange (Zhou et al., 2006), Methylene Blue (Zhang et al., 2007; Jiang et al., 2008; Yao et al., 2008), and Rhodamine B (Zhang et al., 2006), and for the evolution of O_2 from aqueous silver nitrate solutions (Yu and Kudo, 2006; Zhang et al., 2008) under visible-light illumination. $BiVO_4$ has three crystal phases of tetragonal zircon, monoclinic scheelite, and tetragonal scheelite, among which the monoclinic scheelite $BiVO_4$ with a bandgap energy of 2.4 eV is the most active photocatalytically under visible-light irradiation (Tokunaga et al., 2001). Several methods, such as solid-state reaction (Sleight et al., 1979), coprecipitation (Yu et al., 2009), hydrothermal treatment (Zhao et al., 2008), chemical bath deposition (Neves and Trindade, 2002), organometallic decomposition (Sayama et al., 2003), and sonochemical routes (Zhou et al., 2006), have been reported for the fabrication of monoclinic scheelite $BiVO_4$. Among these strategies, the hydrothermal one is a simple and effective pathway in generating monoclinic $BiVO_4$ with perfect crystal structures and regular morphologies in an environmentally benign manner (Yu and Kudo, 2006). Up to now, a large number of monoclinic $BiVO_4$ with various morphologies have been fabricated using the hydrothermal method. For example, a series of monoclinic $BiVO_4$ with hyperbranched structures could be synthesized by hydrothermally treating the mixture of $Bi(NO_3)_3$ and Na_3VO_4 at 200°C under acidic conditions (Zhao et al., 2008). With $Bi(NO_3)_3$ and NH_4VO_3 as starting material and urea or ammonia as pH adjusting agent, highly crystalline monoclinic $BiVO_4$ powders with polyhedral and rod-like morphologies could be generated via the hydrothermal route (Yu and Kudo, 2006).

* Corresponding author. E-mail: hxdai@bjut.edu.cn

Monoclinically crystallized $BiVO_4$ nanosheets could be fabricated hydrothermally with sodium dodecylbenzene sulfonate as morphology-directing template (Zhang et al., 2006). By controlling the pH values of the reaction suspensions and with Bi_2O_3 and NH_4VO_3 as inorganic source, cuboid-like, square plate-like, and flower-like $BiVO_4$ could be synthesized via the cetyltrimethylammonium bromide (CTAB)-assisted hydrothermal route (Li et al., 2009a). With the assistance of a surfactant (e.g., hexadecyl trimethyl ammonium bromide, polyvinyl alcohol or polyvinyl pyrrolidone (PVP)), monoclinic $BiVO_4$ materials with flower-, sphere-, and flat bread-like shapes could be synthesized hydrothermally using bismuth nitrate and ammonium metavanadate as metal source (Zhang and Zhang, 2009).

To the best of our knowledge, it is the first time to fabricate spherical $BiVO_4$ material with a porous structure. Previously, our group investigated the fabrication and physicochemical properties of a number of porous and/or nano/microstructured materials, such as mesoporous MgO (Wang et al., 2008) and CaO (Liu et al., 2008), and three-dimensional (3D) ordered macroporous γ-Al_2O_3 and $Ce_{1-x}Zr_xO_2$ with mesoporous walls (Li et al., 2009b), via the surfactant (e.g., Pluronic P123 ($PEO_{20}PPO_{70}PEO_{20}$), F127 ($PEO_{106}PPO_{70}PEO_{106}$), CTAB or polyethylene glycol)-assisted hydrothermal route. Recently, our group extended our attention to the controlled generation and photocatalytic applications of visible-light-driven $BiVO_4$ single crystallites with well-defined morphologies, and found that such morphological single crystalline materials performed well in the photocatalytic degradation of Methylene Blue (MB) (Meng et al., 2011). In this work, we report the controllable fabrication, characterization, and photocatalytic properties of monoclinic $BiVO_4$ with various morphologies and/or porous structures for the degradation of Methyl Orange (MO) under visible-light illumination.

1 Experimental

1.1 Catalyst fabrication

The $BiVO_4$ catalysts with different morphologies were fabricated by adopting the hydrothermal strategy with $Bi(NO_3)_3{\cdot}5H_2O$ and NH_4VO_3 as inorganic source in the presence or absence of poly(vinyl pyrrolidone) (PVP). The typical fabrication procedure was as follows: 10 mmol of well-ground $Bi(NO_3)_3{\cdot}5H_2O$ powders and 10 mmol of well-ground NH_4VO_3 powders were dissolved in 50 mL of HNO_3 aqueous solution (2 mol/L) under stirring. PVP amout of 0.75 or 1.25 g (Bi/PVP molar ratio = 1/0.0025 or 1/0.0042) was added to the above mixed solution. A certain amount of urea or $NaHCO_3$ powders was added to adjust the pH value of the solution to 2–8. After that, 80 mL of the above mixture (a certain amount of deionized water was added if the volume of the mixture was less than 80 mL) was transferred into a 100-mL Teflon-lined stainless steel autoclave for hydrothermal treatment at 100 or 160°C for 30 hr. The as-obtained yellow precipitate was in turn filtered, washed with deionized water and absolute ethanol three times, dried at 60°C for 12 hr, and calcined at a ramp of 1°C/min from room temperature to 550°C and kept at this temperature for 4 hr in a muffle furnace, thus generating the $BiVO_4$ catalyst. For the sake of clear presentation, we denote the catalysts fabricated under various conditions as $BiVO_4$-x (x = 1–4), as described in Table 1.

All of the chemicals (A.R. in purity) were purchased from Beijing Chemical Company and used without further purification.

1.2 Catalyst characterization

X-ray diffraction patterns of the $BiVO_4$ samples were recorded on an X-ray diffractometer (Bruker/AXS D8 Advance, Germany) with a Cu K_α X-ray irradiation source (λ = 0.15406 nm). Laser Raman spectra of the $BiVO_4$ samples were measured on a Raman spectrometer (Bruker RFS/100, Germany) equipped with a Nd:YAG laser (1064 nm) and an InGaAs detector; the laser power was 100 mW. The powdered samples were placed in a sample holder, and recorded from 200 to 1000 cm^{-1} with a resolution of 4 cm^{-1} in ambient atmosphere. Thermogravimetric analysis and differential scanning calorimetric analysis for the uncalcined sample were conducted in an air flow of 100 mL/min at a ramp of 10°C/min from room temperature to 900°C on a SDT Q600 instrument (TA, USA). Surface areas of the samples were determined on an adsorption analyzer (Micromeritics ASAP 2020, USA) via N_2 adsorption at –196°C. Before measurement, the samples were degassed at 250°C for 3 hr. The surface areas were calculated by using the Brunauer-Emmett-Teller method. Morphologies of the sample particles were determined on a scanning electron microscopic (Gemini Zeiss Supra 55, Germany) apparatus operated at 10 kV. Transmission electron microscopic images of the typical sample were recorded on a JEOL JEM-2010 apparatus, (Japan). The X-ray photoelectron spectroscopy (XPS) was used to determine the Bi 4f, V 2p, and O 1s binding energies (BEs) of surface bismuth, vanadium, and oxygen species, respectively; Mg K_α ($h\nu$ = 1253.6 eV) was the excitation source. Before XPS measurement, the sample was treated in an O_2 flow of 20 mL/min at 550°C for

Table 1 Fabrication parameters, crystal structures, morphologies, BET surface areas, and bandgap energies of the $BiVO_4$ catalysts

Catalyst code	Surfactant[a]	Alkaline source	pH	Crystal structure	Morphology	Surface area (m^2/g)	Bandgap energy (eV)
$BiVO_4$-1	PVP	$CO(NH_2)_2$	2	Monoclinic	Porous spherical	8.4	2.45
$BiVO_4$-2	PVP	$CO(NH_2)_2$	2	Monoclinic	Porous spherical	5.0	2.49
$BiVO_4$-3	–	$NaHCO_3$	7	Monoclinic	Flower-cluster-like	2.4	2.52
$BiVO_4$-4	–	$NaHCO_3$	8	Monoclinic	Flower-bundle-like	3.2	2.52

[a] Bi/PVP molar ratio was 1/0.0025 for $BiVO_4$-1 and 1/0.0042 for $BiVO_4$-2.

1 hr. After being cooled to room temperature and by means of a glove bag (Instruments for Research and Industry, USA), the sample was transferred into the spectrometer under helium. The sample was outgassed (0.5 hr) in the preparation chamber before being analyzed in the analysis chamber. The C 1s signal at 284.6 eV was taken as a reference for BE calibration. The ultraviolet-visible (UV-Vis) diffuse reflectance spectra of the samples in the 200–900 nm range were recorded on a Shimadzu UV-2450 spectrophotometer (Japan) using $BaSO_4$ as standard.

1.3 Photocatalytic evaluation

Photocatalytic activities of the $BiVO_4$ samples were evaluated for the degradation of MO under visible-light illumination in a quartz reactor (QO250, Beijing Changtuo Sci. & Technol. Co., Ltd., China). A 300-W Xe lamp was used as light source and an optical cut-off filter was employed to only permit the illumination of light with wavelength of > 400 nm. The photocatalytic evaluation experiments were performed at ambient temperature as follows: 0.1 g of the $BiVO_4$ or P25 (TiO_2) sample was added to 200 mL of MO solution (initial MO concentration C_0 = 1.0×10^{-5} mol/L); after being ultrasonicated for 0.5 hr, the mixed solution was magnetically stirred for 3 hr to reach the adsorption-desorption equilibrium. The temperature of the reaction system was kept at ca. 25°C using flowing cool water. A small amount (4 mL) of the reactant solution was taken at 20-min intervals and separated by centrifugation for MO concentration determination. The MO concentration (C_t) after a certain reaction time (t) was determined by measuring the absorbance of the reactant solution at 464 nm during the photocatalytic degradation process on the aforementioned UV-Vis equipment. The C_t/C_0 ratio was used to evaluate the photocatalytic performance of the sample.

2 Results and discussion

2.1 Crystal structure and surface area

Figure 1 illustrates the TGA/DSC profiles of the typical sample ($BiVO_4$-1) before calcination. There was a small weight loss (ca. 0.32 wt.%) appeared below 184°C, ascribable to the removal of the adsorbed water, accompanying by the appearance of an endothermic signal centered at 169°C. Two weight losses (ca. 0.16 wt.% in the 184–226°C range and ca. 1.28 wt.% in the 226–386°C range) were caused by the removal of the nitrates and PVP left after washing with water and ethanol, companying by the detection of two exothermic signals centered at 207 and 271°C, respectively. Therefore, it was appropriate to calcine the $BiVO_4$ precursors at 550°C for the total elimination of surfactant molecules and the formation of single-phase monoclinic $BiVO_4$ phases (substantiated by the XRD results below).

Figure 2 shows the XRD patterns of the $BiVO_4$ samples obtained under various conditions. All of the diffraction peaks of the $BiVO_4$ samples could be well indexed to the monoclinic scheelite phase (JCPDS PDF# 83–1700), as

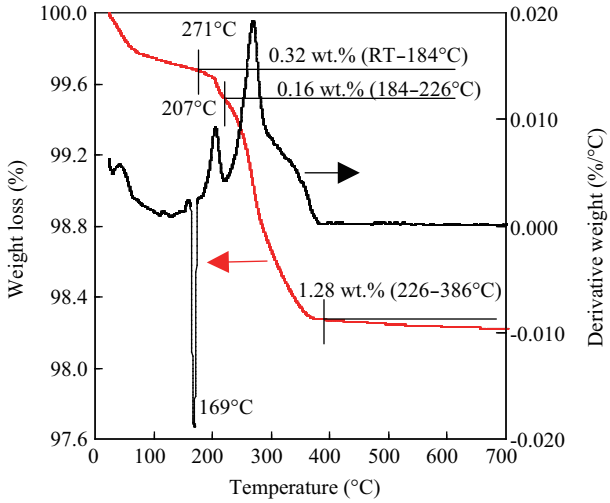

Fig. 1 TGA/DSC profiles of the $BiVO_4$-1 sample before calcination at 550°C for 4 hr. RT: room temperature.

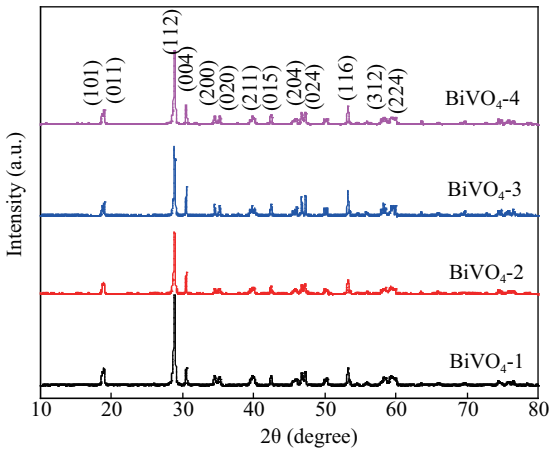

Fig. 2 XRD patterns of the $BiVO_4$ samples.

indicated in Fig. 2. No other peaks assignable to impurity phases were detected. Other authors have also obtained similar XRD patterns of $BiVO_4$ (Tokunaga et al., 2001; Ke et al., 2008; Huang et al., 2010; Zhang et al., 2010). The formation of monoclinic scheelite $BiVO_4$ structure was substantiated by the results of laser Raman studies (Fig. 3). It can be seen from Fig. 3 that there were Raman bands at ca. 210, 327, 367, 633, 702, and 826 cm^{-1} for all of

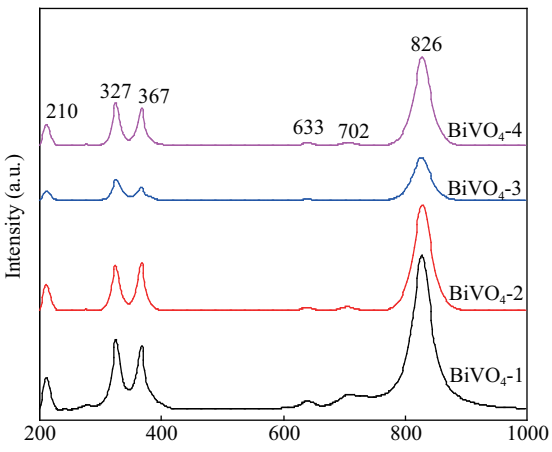

Fig. 3 Laser Raman spectra of the $BiVO_4$ samples.

the samples. These signals were the characteristic Raman bands of monoclinic $BiVO_4$. The most intense band at ca. 826 cm^{-1} was attributed to the symmetric V–O stretching mode and the weak bands at ca. 702 and 633 cm^{-1} were assigned to the asymmetric V–O stretching mode. The asymmetric and symmetric bending vibrations of the VO_4 tetrahedron were detected at ca. 327 and 367 cm^{-1}, respectively. The external mode (rotation/translation) occurred at ca. 210 cm^{-1} (Hardcastle et al., 1991). The V–O stretching mode (at ca. 822 cm^{-1}) of the $BiVO_4$-3 sample shifted to a lower frequency compared to that (at ca. 826 cm^{-1}) of the other $BiVO_4$ samples, indicating that the bond length of the $BiVO_4$-3 sample was longer (Yu and Kudo, 2006). The differences in width and intensity of the Raman bands in the $BiVO_4$ samples reflected the variations in crystallinity, defect and disorder, particle size, and/or particle aggregation of these materials (Zhang et al., 2009). The results of the Raman investigations indicate that the fabrication parameters had an important effect on the crystallinity and particle morphology of the $BiVO_4$ samples. From Fig. 2, one can also observe that there was a discrepancy in peak intensity of the $BiVO_4$ samples, indicating the presence of crystallinity difference among these samples. All of the four samples were single-phase monoclinic scheelite $BiVO_4$, implying that the calcination temperature (550°C) was appropriate to guarantee the generation of single-phase monoclinic scheelite $BiVO_4$.

A number of investigations have shown that surface area of a photocatalyst has a positive effect on the enhancement in photocatalytic performance (Amano et al., 2008; Ai et al., 2010; Li et al., 2008). Although $BiVO_4$ materials with high surface areas (40–60 m^2/g) were fabricated via the KIT-6-nanocasting route (Li et al., 2008) and via the flame-assisted synthesis route (Castillo et al., 2010), most of monoclinic $BiVO_4$ catalysts reported in the literature possessed a lower surface area (< 3 m^2/g) (Zhang et al., 2010), due to the high-temperature calcination processes adopted. Table 1 summarizes the surface areas of the $BiVO_4$ samples. It is observed that the $BiVO_4$-1 and $BiVO_4$-2 samples derived with the addition of PVP and urea exhibited a higher surface area of 8.4 and 5.0 m^2/g, respectively; but the $BiVO_4$ sample obtained in the absence of PVP with urea showed a much lower surface area (1.9 m^2/g). As for the $BiVO_4$-3 and $BiVO_4$-4 samples fabricated in the absence of PVP and with $NaHCO_3$ as pH adjustor, the surface areas (2.4 and 3.2 m^2/g, respectively) were also lower. Obviously, the surfactant PVP played a crucial role in generating high-surface-area monoclinic $BiVO_4$ materials.

2.2 Morphology and formation mechanism

Figure 4 shows the SEM and TEM images of the $BiVO_4$ samples. It is observed that the $BiVO_4$-1 and $BiVO_4$-2 samples derived with PVP as surfactant and urea as pH regulator (pH = 2) were composed of spherical microparticles with pores on the surface and in the inner (Fig. 4a, b, and i). The diameter of the spherical $BiVO_4$-1 particles was 3–4 μm, smaller than that (4–6 μm) of the $BiVO_4$-2 particles. Although hollow $BiVO_4$ nanospheres without pore structures could be fabricated with colloidal carbon spheres as hard template (Yin et al., 2009), spherical $BiVO_4$ materials with porous architectures have not been reported before. In the absence of PVP with $NaHCO_3$ as pH adjustor (pH = 7 or 8), the obtained $BiVO_4$-3 and $BiVO_4$-4 samples displayed significantly different morphologies; the former showed a flower-cluster-like shape that was composed of a number of spindle-like microrods (Fig. 4e and f). The $BiVO_4$ particles with a similar morphology were also generated by other research (Su et al., 2010). When the pH value rose from 7 to 8, the obtained $BiVO_4$-4 sample exhibited a flower-bundle-like morphology with some cavities on the surfaces (Fig. 4g and h), and each piece of a bundle was compiled by numerous nano/microsized pseudo-cubes (about 1 μm in diameter). Zhang et al. (2009) ever pointed out that there was presence of significant effect of pH value on the morphology of $BiVO_4$ photocatalyst derived via a hydrothermal route. Obviously, the big difference in particle morphology of our four $BiVO_4$ samples was associated with the PVP and pH value during the fabrication process.

The above SEM observations reveal that surfactant and pH value had an important role to play in the morphological evolution of $BiVO_4$ particles. When the pH value of the precursor solution was adjusted to 7 or 8 with $NaHCO_3$, the vanadium and bismuth were present in the forms of VO_3^- and Bi^{3+} (Zhang et al., 2009), respectively; during the hydrothermal process VO_3^- and Bi^{3+} could react to generate $BiVO_4$ crystal nuclei, which then grew up to produce primary $BiVO_4$ nanoparticles, and these nanoparticles finally aggregated to form rod- or cube-like structures according to the "oriented attachment" mechanism (Penn and Banfield, 1998). With the further growth of the subunits, these rods or cubes were aligned to crystallize into flower-cluster-like ($BiVO_4$-3) or flower-bundle-like ($BiVO_4$-4) microentities through the Ostwald ripening process after calcination at 550°C. In the PVP-mediated hydrothermal processes, however, only irregular aggregations of nanoparticles were obtained in the absence of PVP (not shown here). Obviously, PVP played an important role in the formation of porous spherical $BiVO_4$ microentities. In the presence of PVP in the precursor solution, these PVP molecules could adsorb on the initially formed $BiVO_4$ nanoparticles. Although the absorbed PVP molecules prevented the primary nanoparticles from growth (Cheng et al., 2009), these PVP-covered primary $BiVO_4$ nanoparticles could interact in all directions to self-assemble to form a spherical alignment, which then transferred into porous spherical $BiVO_4$ microentities after calcination. It should be noted that the presence of the steric effect of PVP molecules (Zhu et al., 2004) would cause the spherically aligned particles to be loosely compiled and numerous pores were hence generated in the external and internal surfaces of each spherical microentitiy (Zhu et al., 2009).

2.3 Metal oxidation state, oxygen vacancy density, and surface composition

The Bi 4f, V $2p_{3/2}$, and O 1s XPS spectra of the $BiVO_4$ samples are shown in Fig. 5. It is observed that the Bi 4f

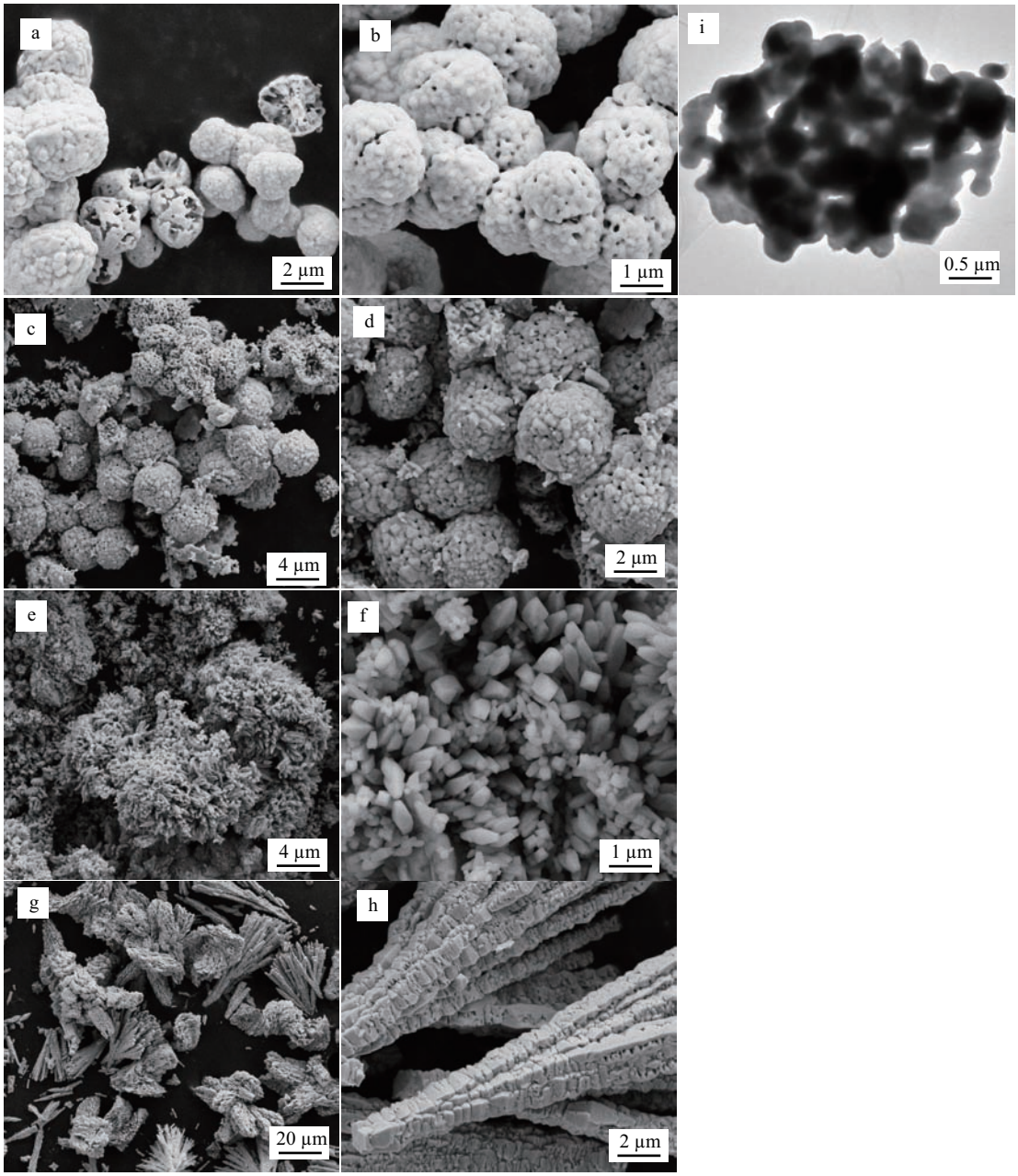

Fig. 4 SEM (a, b) and TEM (i) images of $BiVO_4$-1, and SEM images of $BiVO_4$-2 (c, d), $BiVO_4$-3 (e, f), and $BiVO_4$-4 (g, h).

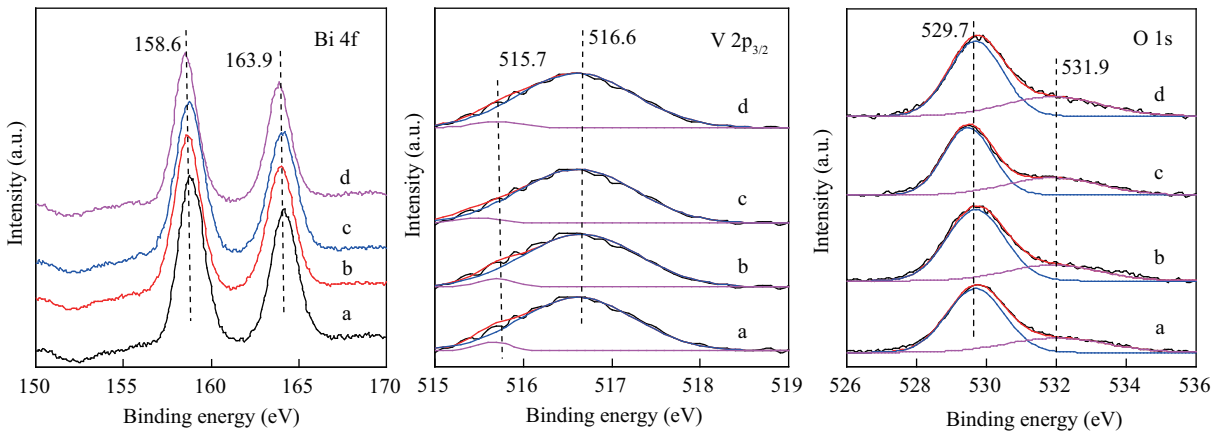

Fig. 5 Bi 4f, V $2p_{3/2}$, and O 1s XPS spectra of the $BiVO_4$ samples. Line a $BiVO_4$-1; line b $BiVO_4$-2; line c $BiVO_4$-3; line d $BiVO_4$-4.

spectrum of each $BiVO_4$ sample showed two symmetric peaks at BE = 158.6 and 163.9 eV (assignable to the spin-orbit splitting of Bi $4f_{7/2}$ and $4f_{5/2}$, respectively), which were characteristic signals of Bi^{3+} (Zhang et al., 2006;

Jiang et al., 2009). This result indicates that all of the bismuth ions in the $BiVO_4$ samples existed in trivalency. Similar results were also reported by other publications (Zhang et al., 2006; Jiang et al., 2009). As can bee seen from Fig. 5, the asymmetric V $2p_{3/2}$ peak could be decomposed into two components at BE = 516.6 and 515.7 eV, attributable to the surface V^{5+} and V^{4+} species (Liu et al., 2007), respectively. In other words, there was co-presence of V^{5+} (in majority) and V^{4+} (in minority) species in the $BiVO_4$ samples. In terms of the electroneutrality principle, it can be deduced that the $BiVO_4$ samples were oxygen-deficient (i.e., $BiVO_{4-\delta}$) and the surface nonstoichiometric oxygen amount (δ) depended upon the surface V^{4+}/V^{5+} molar ratio. As for the O 1s spectra of the $BiVO_4$ samples, the asymmetric peak centered at ca. 530 eV could be deconvoluted to two components at BE = 529.7 and 531.9 eV, ascribable to surface lattice oxygen (O^{2-}_{latt}) and adsorbed oxygen (O_{ads}) species, respectively (Kulkarni et al., 1995). Since the $BiVO_4$ samples were pretreated in an O_2 flow at 550°C before the recording of XPS spectra, the possibility of surface OH^- and CO_3^{2-} species existence would be minimized. Therefore, the O_{ads} species were mainly O^-, O_2^- or O_2^{2-} species, which dwelled at the surface oxygen vacant sites of the $BiVO_{4-\delta}$ samples (Kulkarni et al., 1995). Table 2 summarizes the surface Bi/V, V^{4+}/V^{5+}, and O_{ads}/O^{2-}_{latt} molar ratios of the $BiVO_4$ samples. The surface Bi/V molar ratios (0.98–1.07) of all of the $BiVO_4$ samples were close to 1, indicating that these samples were homogeneous $BiVO_4$ phase. The surface V^{4+}/V^{5+} and O_{ads}/O^{2-}_{latt} molar ratios reveal that the $BiVO_4$-1 and $BiVO_4$-2 samples possessed more amounts of surface V^{4+} and O_{ads} species than the $BiVO_4$-3 and $BiVO_4$-4 samples. In other words, the former two samples contained more amounts of surface oxygen vacancies (i.e., higher surface oxygen vacancy density) than the latter two samples. It is well known that a higher oxygen vacancy density would be beneficial for the enhancement in photocatalytic performance, as substantiated by the activity data shown later.

Table 2 Surface Bi/V, V^{4+}/V^{5+}, and O_{ads}/O^{2-}_{latt} molar ratios of the as-fabricated $BiVO_4$ samples

Sample code	Bi/V molar ratio	V^{4+}/V^{5+} molar ratio	O_{ads}/O^{2-}_{latt} molar ratio
$BiVO_4$-1	1.01	0.050	0.489
$BiVO_4$-2	0.98	0.048	0.466
$BiVO_4$-3	1.06	0.036	0.352
$BiVO_4$-4	1.07	0.043	0.389

2.4 Optical absorption behavior

Figure 6 illustrates the UV-Vis DRS spectra of the $BiVO_4$ samples. All of the samples exhibited strong absorption in the UV- and visible-light regions, which was characteristic of monoclinic $BiVO_4$ (Zhou et al., 2010). The steep shape of each spectrum in the visible-light range was due to the bandgap transition (Zhou et al., 2007). For a crystalline semiconductor, the optical absorption near the band edge follows the formula of $(\alpha h\nu)^2 = A(h\nu - E_g)^n$, where α, $h\nu$, A, and E_g denote the adsorption coefficient, incident photon energy, constant, and bandgap energy, respectively. Among them, the value of n depends upon the characteristics of the transition, i.e., direction transition ($n = 1$) and indirection transition ($n = 4$). The n value for $BiVO_4$ is 1 (Zhou et al., 2006). Therefore, the E_g value of each $BiVO_4$ sample could be estimated from the intercept of the plot $(\alpha h\nu)^2$ versus $h\nu$, as summarized in Table 1. The bandgap energies of the $BiVO_4$ samples were in the range of 2.45–2.52 eV, which were comparable to those reported by other investigators (Li et al., 2009; Shen et al., 2010). Compared to the $BiVO_4$-3 and $BiVO_4$-4 samples, the spherical $BiVO_4$-1 and $BiVO_4$-2 samples with porous structures possessed lower bandgap energies (2.45–2.49 eV), indicating that the porous $BiVO_4$ samples could respond to visible light more effectively and would hence be expected to show higher visible-light-driven photocatalytic performance, as confirmed by the photocatalytic evaluation results below.

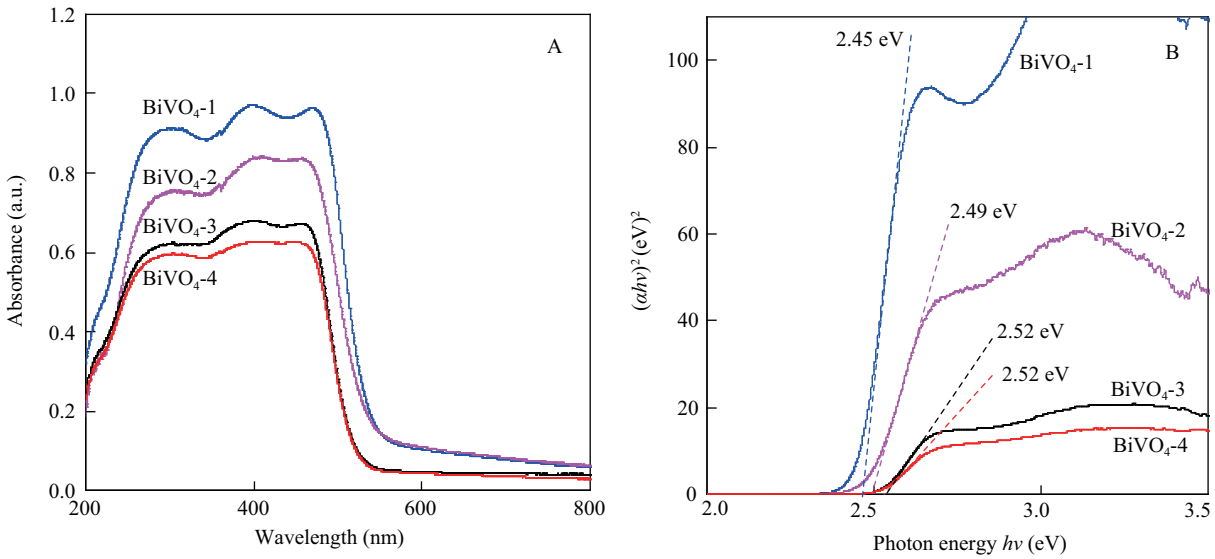

Fig. 6 UV-Vis diffuse reflectance spectra (A) and plots of the $(\alpha h\nu)^2$ versus $h\nu$ (B) of $BiVO_4$ samples.

2.5 Photocatalytic performance

The photocatalytic performance of the $BiVO_4$ samples was determined for the degradation of MO in an aqueous solution under visible-light illumination. For comparison purposes, the experiments of MO direct photolysis (blank experiment) and MO degradation over the commercial TiO_2 (Degussa P25) nanoparticles under identical conditions were also carried out. Figure 7 shows the MO concentration ratios (C_t/C_0) of the different samples and that of the direct photolysis process with irradiation time. Obviously, the MO concentration in the blank experiment was slightly changed after visible-light irradiation for 2 hr, indicating that MO could hardly be photolyzed under this condition. Similar phenomena were also observed by other authors (Ge, 2008). Over the P25 sample, the MO conversion after visible-light irradiation for 2 hr was ca. 7%. The $BiVO_4$ samples, however, exhibited much better visible-light-driven photocatalytic performance than the P25 sample, and the MO conversion within 2 hr of reaction decreased in the order of $BiVO_4$-1 (84%) > $BiVO_4$-2 (65%) > $BiVO_4$-4 (44%) > $BiVO_4$-3 (30%). The degradation rate (4.20×10^{-5} $mol_{MO}/(g_{cat}\cdot hr)$) obtained over $BiVO_4$-1 was significantly higher than that (1.07×10^{-5} $mol_{MO}/(g_{cat}\cdot hr)$) obtained over the $BiVO_4$ material reported elsewhere (Zhang and Zhang, 2010). Apparently, the spherical $BiVO_4$-1 and $BiVO_4$-2 samples with porous structures were much superior to the flower-cluster-like $BiVO_4$-3 and flower-bundle-like $BiVO_4$-4 samples in photocatalytic performance. It has been generally accepted that photocatalytic performance is mainly influenced by the factors, such as adsorption capacity of reactants, ability of optical absorption, and separation and transportation rates of photogenerated electrons and holes in the catalyst (Chang et al., 2007). In our previous studies, we observed a drop in bandgap energy of $BiVO_4$ (Jiang et al., 2011) or Fe_2O_3 (Zhang et al., 2011) with a porous structure. It is known that a higher surface area and a developed porous architecture facilitate the adsorption of reactant molecules, and the presence of oxygen vacancies is beneficial for the activation of oxygen molecules dissolved in the solution to active oxygen species, which was helpful for the separation of photogenerated electrons and holes in catalyst. Therefore, the co-action of these factors would give rise to the enhancement in photocatalytic performance. Compared to the $BiVO_4$-3 and $BiVO_4$-4 samples, the $BiVO_4$-1 and $BiVO_4$-2 samples possessed higher surface areas, stronger photoabsorptive ability, and narrower bandgap energies (Table 1, Fig. 6). Furthermore, higher surface oxygen vacancy densities in the $BiVO_4$-1 and $BiVO_4$-2 samples than those in the $BiVO_4$-3 and $BiVO_4$-4 samples might also contribute to the improved photocatalytic performance of the former two catalysts. In addition, the porous structures of $BiVO_4$-1 and $BiVO_4$-2 could favor the adsorption and diffusion of reactants as well as the facile accessibility of incident light to more surfaces of catalysts, thus leading to an enhancement in photocatalytic activity (Sun et al., 2009).

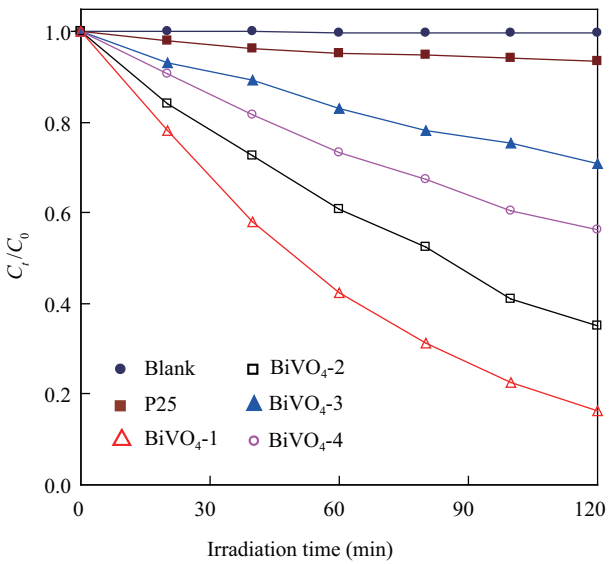

Fig. 7 Photocatalytic activities of the blank (direct photolysis), Degussa P25, and $BiVO_4$ samples for the degradation of MO under visible-light (λ > 400 nm) irradiation.

3 Conclusions

Monoclinic scheelite $BiVO_4$ materials with multiple morphologies and/or porous structures were fabricated by using the hydrothermal method with bismuth nitrate and ammonium metavanadate as inorganic source, urea or $NaHCO_3$ as pH adjustor, and/or the PVP as surfactant. The results revealed that surfactant and pH value had a great impact on the morphology and pore structure of the $BiVO_4$ product. Spherical $BiVO_4$ with porous structures, flower-cluster-like $BiVO_4$, and flower-bundle-like $BiVO_4$ could be fabricated hydrothermally at 100°C with PVP and urea (pH = 2) and at 160°C with $NaHCO_3$ (pH = 7 and 8), respectively. The surface areas and bandgap energies of the four $BiVO_4$ samples were in the range of 2.4–8.4 m^2/g and 2.45–2.52 eV, respectively. Among the four samples, the spherical $BiVO_4$ with a surface area of 8.4 m^2/g showed the highest photocatalytic activity for the degradation of MO under visible-light irradiation, which might be due to its higher surface area, lower bandgap energy, higher surface oxygen vacancy density, and unique porous architecture.

Acknowledgements

The work was supported by the National Natural Science Foundation of China (No. 20973017, 21077007), the Creative Research Foundation of Beijing University of Technology (No. 00500054R4003, 005000543111501), the Hi-Tech Research and Development Program (863) of China (No. 2009AA063201), and the Funding Project for Academic Human Resources Development in Institutions of Higher Learning under the Jurisdiction of Beijing Municipality (No. PHR200907105, PHR201007105, PHR201107104). C. T. Au thanks for the financial support from the Hong Kong Baptist University (FRG2/09-10/023). We also thank Jianping He (State Key Laboratory of Advanced Metals and Materials, University of Science & Technology Beijing) for doing the SEM analysis of the samples.

References

Ai Z H, Ho W K, Lee S C, Zhang L Z, 2009. Efficient photocatalytic removal of NO in indoor air with hierarchical bismuth oxybromide nanoplate microspheres under visible light. *Environmental Science and Technology*, 43(11): 4143–4150.

Ai Z H, Zhang L Z, Lee S C, 2010. Efficient visible light photocatalytic oxidation of NO on aerosol flow-synthesized nanocrystalline $InVO_4$ hollow microspheres. *The Journal of Physical Chemistry C*, 114(43): 18594–18600.

Amano F, Yamakata A, Nogami K, Osawa M, Ohtani B, 2008. Visible light responsive pristine metal oxide photocatalyst: enhancement of activity by crystallization under hydrothermal treatment. *Journal of the American Chemical Society*, 130(53): 17650–17651.

Castillo N C, Heel A, Graule T, Pulgarin C, 2010. Flame-assisted synthesis of nanoscale, amorphous and crystalline, spherical $BiVO_4$ with visible-light photocatalytic activity. *Applied Catalysis B: Environmental*, 95(3-4): 335–347.

Chang W K, Rao K K, Kuo H C, Cai J F, Wong M S, 2007. A novel core-shell like composite In_2O_3@$CaIn_2O_4$ for efficient degradation of methylene blue by visible light. *Applied Catalysis A: General*, 321(1): 1–6.

Chen Y, Dionysiou D D, 2006. Effect of calcination temperature on the photocatalytic activity and adhesion of TiO_2 films prepared by the P-25 powder-modified sol-gel method. *Journal of Molecular Catalysis A: Chemical*, 244(1-2): 73–82.

Cheng G, Wu J L, Xiao F, Yu H, Lu Z, Yu X L et al., 2009. Synthesis of bismuth micro- and nanospheres by a simple refluxing method. *Materials Letters*, 63(26): 2239–2242.

Ge L, 2008. Novel Pd/$BiVO_4$ composite photocatalysts for efficient degradation of methyl orange under visible light irradiation. *Materials Chemistry and Physics*, 107(2-3): 465–470.

Hardcastle F D, Wachs I E, Eckert H, Jefferson D A, 1991. Vanadium(V) environments in bismuth vanadates: A structural investigation using Raman spectroscopy and solid state ^{51}V NMR. *Journal of Solid State Chemistry*, 90(2): 194–210.

Hoffmann M R, Martin S T, Choi W, Bahnemann D W, 1995. Environmental applications of semiconductor photocatalysis. *Chemical Reviews*, 95(1): 69–96.

Huang C M, Pan G T, Peng P Y, Yang T C K, 2010. In situ DRIFT study of photocatalytic degradation of gaseous isopropanol over $BiVO_4$ under indoor illumination. *Journal of Molecular Catalysis A: Chemical*, 327(1-2): 38–44.

Jiang H Q, Endo H, Natori H, Nagai M, Kobayashi K, 2008. Fabrication and photoactivities of spherical-shaped $BiVO_4$ photocatalysts through solution combustion synthesis method. *Journal of the European Ceramic Society*, 28(15): 2955–2962.

Jiang H Q, Nagai M, Kobayashi K, 2009. Enhanced photocatalytic activity for degradation of methylene blue over V_2O_5/$BiVO_4$ composite. *Journal of Alloys and Compounds*, 479(1-2): 821–827.

Jiang H Y, Dai H X, Meng X, Zhang L, Deng J G, Ji K M, 2011. Porous olive-like $BiVO_4$: Alcoho-hydrothermal preparation and excellent visible-light-driven photocatalytic performance for the degradation of phenol. *Applied Catalysis B: Environmental*, 105(3-4): 326–334.

Ke D N, Peng T Y, Ma L, Cai P, Jiang P, 2008. Photocatalytic water splitting for O_2 production under visible-light irradiation on $BiVO_4$ nanoparticles in different sacrificial reagent solutions. *Applied Catalysis A: General*, 350(1): 111–117.

Kulkarni G U, Rao C N R, Roberts M W, 1995. Nature of the oxygen species at Ni(110) and Ni(100) surfaces revealed by exposure to oxygen and oxygen-ammonia mixtures: Evidence for the surface reactivity of O^- type species. *The Journal of Physical Chemistry*, 99(10): 3310–3316.

Li H B, Liu G C, Duan X C, 2009a. Monoclinic $BiVO_4$ with regular morphologies: hydrothermal synthesis, characterization and photocatalytic properties. *Materials Chemistry and Physics*, 115(1): 9–13.

Li H N, Zhang L, Dai H X, He H, 2009b. Facile synthesis and unique physicochemical properties of three-dimensionally ordered macroporous magnesium oxide, gamma-alumina, and ceria-zirconia solid solutions with crystalline mesoporous walls. *Inorganic Chemistry*, 48(10): 4421–4434.

Li G S, Zhang D Q, Yu J C, 2008. Ordered mesoporous $BiVO_4$ through nanocasting: A superior visible light-driven photocatalyst. *Chemistry of Materials*, 20(12): 3983–3992.

Liu C X, Zhang L, Deng J G, Mu Q, Dai H X, He H, 2008. Surfactant-aided hydrothermal synthesis and carbon dioxide adsorption behavior of three-dimensionally mesoporous calcium oxide single-crystallites with tri-, tetra-, and hexagonal morphologies. *The Journal of Physical Chemistry C*, 112(49): 19248–19256.

Liu W, Lai S Y, Dai H X, Wang S J, Sun H Z, Au C T, 2007. Oxidative dehydrogenation of *n*-butane over mesoporous VO_x/SBA-15 catalysts. *Catalysis Letters*, 113(3-4): 147–154.

Meng X, Zhang L, Dai H X, Zhao Z X, Zhang R Z, Liu Y X, 2011. Surfactant-assisted hydrothermal fabrication and visible-light-driven photocatalytic degradation of methylene blue over multiple morphological $BiVO_4$ single-crystallites. *Materials Chemistry and Physics*, 125(1-2): 59–65.

Neves M C, Trindade T, 2002. Chemical bath deposition of $BiVO_4$. *Thin Solid Films*, 406(1-2): 93–97.

Penn R L, Banfield J F, 1998. Imperfect oriented attachment: dislocation generation in defect-free nanocrystals. *Science*, 281(5379): 969–971.

Sayama K, Nomura A, Zou Z G, Abe R, Abe Y, Arakawa H, 2003. Photoelectrochemical decomposition of water on nanocrystalline $BiVO_4$ film electrodes under visible light. *Chemical Communications*, 35(8): 2908–2909.

Shen Y, Huang M L, Huang Y, Lin J M, Wu J H, 2010. The synthesis of bismuth vanadate powders and their photocatalytic properties under visible light irradiation. *Journal of Alloys and Compounds*, 496(1-2): 287–292.

Sleight A W, Chen H Y, Ferretti A, Cox D E, 1979. Crystal growth and structure of $BiVO_4$. *Materials Research Bulletin*, 14(12): 1571–1581.

Su J Z, Guo L J, Yoriya S, Grimes C A, 2010. Aqueous growth of pyramidal-shaped $BiVO_4$ nanowire arrays and structural characterization: application to photoelectrochemical water splitting. *Crystal Growth & Design*, 10(2): 856–861.

Sun M, Li D Z, Zhang W J, Chen Z X, Huang H J, Li W J et al., 2009. Photocatalyst $Cd_2Sb_2O_{6.8}$ with high photocatalytic activity toward benzene and dyes. *The Journal of Physical Chemistry C*, 113(33): 14916–14921.

Tokunaga S, Kato H, Kudo A, 2001. Selective preparation of monoclinic and tetragonal $BiVO_4$ with scheelite structure and their photocatalytic properties. *Chemistry of Materials*, 13(12): 4624–4628.

Wang G Z, Zhang L, Dai H X, Deng J G, Liu C X, He H et al., 2008. P123-assisted hydrothermal synthesis and character-

ization of rectangular parallelepiped and hexagonal prism single-crystalline MgO with three-dimensional wormhole-like mesopores. *Inorganic Chemistry*, 47(10): 4015–4022.

Xu H, Li H M, Wu C D, Chu J Y, Yan Y S, Shu H M et al., 2008. Preparation, characterization and photocatalytic properties of Cu-loaded $BiVO_4$. *Journal of Hazardous Materials*, 153(1-2): 877–884.

Yao W F, Iwai H, Ye J H, 2008. Effects of molybdenum substitution on the photocatalytic behavior of $BiVO_4$. *Dalton Transactions*, (11): 1426–1430.

Yin W Z, Wang W Z, Shang M, Zhou L, Sun S M, Wang L, 2009. $BiVO_4$ hollow nanospheres: anchoring synthesis, growth mechanism, and their application in photocatalysis. *European Journal of Inorganic Chemistry*, 2009(29-30): 4379–4384.

Yu J Q, Kudo A, 2006. Effects of structural variation on the photocatalytic performance of hydrothermally synthesized $BiVO_4$. *Advanced Functional Materials*, 16(16): 2163–2169.

Yu J Q, Zhang Y, Kudo A, 2009. Synthesis and photocatalytic performances of $BiVO_4$ by ammonia co-precipitation process. *Journal of Solid State Chemistry*, 182(2): 223–228.

Zhang A P, Zhang J Z, 2009. Characterization of visible-light-driven $BiVO_4$ photocatalysts synthesized via a surfactant-assisted hydrothermal method. *Spectrochimica Acta A*, 73(2): 336–341.

Zhang A P, Zhang J Z, 2010. Synthesis and characterization of Ag/$BiVO_4$ composite photocatalyst. *Applied Surface Science*, 256(10): 3224–3227.

Zhang A P, Zhang J Z, Cui N Y, Tie X Y, An Y W, Li L J, 2009. Effects of pH on hydrothermal synthesis and characterization of visible-light-driven $BiVO_4$ photocatalyst. *Journal of Molecular Catalysis A: Chemical*, 304(1-2): 28–32.

Zhang H M, Liu J B, Wang H, Zhang W X, Yan H, 2008. Rapid microwave-assisted synthesis of phase controlled $BiVO_4$ nanocrystals and research on photocatalytic properties under visible light irradiation. *Journal of Nanoparticle Research*, 10(5): 767–774.

Zhang L, Chen D R, Jiao X L, 2006. Monoclinic structured $BiVO_4$ nanosheets: hydrothermal preparation, formation mechanism, and coloristic and photocatalytic properties. *The Journal of Physical Chemistry B*, 110(16): 2668–2673.

Zhang R Z, Dai H X, Du Y C, Zhang L, Deng J G, Xia Y S et al., 2011. P123-PMMA dual-templating generation and unique physicochemical properties of three-dimensionally ordered macroporous iron oxides with nanovoids in the crystalline walls. *Inorganic Chemistry*, 50(6): 2534–2544.

Zhang X, Ai Z H, Jia F L, Zhang L Z, Fan X X, Zou Z G, 2007. Selective synthesis and visible-light photocatalytic activities of $BiVO_4$ with different crystalline phases. *Materials Chemistry and Physics*, 103(1): 162–167.

Zhang Z J, Wang W Z, Shang M, Yin W Z, 2010. Photocatalytic degradation of Rhodamine B and phenol by solution combustion synthesized $BiVO_4$ photocatalyst. *Catalysis Communications*, 11(11): 982–986.

Zhao Y, Xie Y, Zhu X, Yan S, Wang S X, 2008. Surfactant-free synthesis of hyperbranched monoclinic bismuth vanadate and its applications in photocatalysis, gas sensing, and lithium-ion batteries. *Chemistry–A European Journal*, 14(5): 1601–1606.

Zhou L, Wang W Z, Liu S W, Zhang L S, Xu H L, Zhu W, 2006. A sonochemical route to visible-light-driven high-activity $BiVO_4$ photocatalyst. *Journal of Molecular Catalysis A: Chemical*, 252(1-2): 120–124.

Zhou L, Wang W Z, Zhang L S, Xu H L, Zhu W, 2007. Single-crystalline $BiVO_4$ microtubes with square cross-sections: microstructure, growth mechanism, and photocatalytic property. *The Journal of Physical Chemistry C*, 111(37): 13659–13664.

Zhou Y, Vuille K, Heel A, Probst B, Kontic R, Patzke G R, 2010. An inorganic hydrothermal route to photocatalytically active bismuth vanadate. *Applied Catalysis A: General*, 375(1): 140–148.

Zhu H T, Wang J X, Xu G Y, 2009. Fast synthesis of Cu_2O hollow microspheres and their application in DNA biosensor of hepatitis B virus. *Crystal Growth & Design*, 9(1): 633–638.

Zhu H T, Zhang C Y, Yin Y S, 2004. Rapid synthesis of copper nanoparticles by sodium hypophosphite reduction in ethylene glycol under microwave irradiation. *Journal of Crystal Growth*, 270(3-4): 722–728.